




## Article

# High-Temperature Crystal Chemistry of Meta-Autunite Group Minerals: Metatorbernite, $\text{Cu}(\text{UO}_2)_2(\text{PO}_4)_2(\text{H}_2\text{O})_8$ and Metazeunerite, $\text{Cu}(\text{UO}_2)_2(\text{AsO}_4)_2(\text{H}_2\text{O})_8$

Evgeny V. Nazarchuk<sup>1</sup>, Vladislav V. Gurzhiy<sup>1,\*</sup> , Yana G. Tagirova<sup>1</sup>, Dmitri O. Charkin<sup>2</sup>, Maria G. Krzhizhanovskaya<sup>1</sup> , Anatoly V. Kasatkin<sup>3</sup>  and Oleg V. Eremin<sup>4</sup>

<sup>1</sup> Department of Crystallography, Saint-Petersburg State University, University Emb. 7/9, St. Petersburg 199034, Russia; e.nazarchuk@spbu.ru (E.V.N.)

<sup>2</sup> Department of Chemistry, Moscow State University, Vorobievsky Gory 1, bd. 3, Moscow 119991, Russia

<sup>3</sup> Fersman Mineralogical Museum of the Russian Academy of Sciences, Leninskiy pr. 18, 2, Moscow 119071, Russia

<sup>4</sup> Institute of Natural Resources, Ecology and Cryology, Siberian Branch, Russian Academy of Sciences, Nedorezova str. 16a, Chita 672014, Russia

\* Correspondence: vladislav.gurzhiy@spbu.ru

**Abstract:** Thermal expansion of metatorbernite,  $\text{Cu}(\text{UO}_2)_2(\text{PO}_4)_2(\text{H}_2\text{O})_8$  (**1**), and metazeunerite,  $\text{Cu}(\text{UO}_2)_2(\text{AsO}_4)_2(\text{H}_2\text{O})_8$  (**2**), has been investigated using single-crystal and powder X-ray diffraction. Both minerals are prone to dehydration, which proceeds already at ambient conditions. According to the single-crystal XRD data, **1** is stable up to 300(50) K, while **2** is stable up to 250(50) K. Powder XRD studies at various temperatures suggest that **1** dehydrates in three stages at ca. 353, 373, and 483 K, while **2** in two stages at ca. 283 and 543 K. Calculation of the main coefficients of thermal expansion reveals strong anisotropy. The expansion is maximal in the direction normal to the autunite-type layers. This correlates with the anisotropy in thermal evolution of Cu–O bond lengths and differences in the thermal behavior of  $\text{PO}_4$  and  $\text{AsO}_4$  tetrahedra.



**Citation:** Nazarchuk, E.V.; Gurzhiy, V.V.; Tagirova, Y.G.; Charkin, D.O.; Krzhizhanovskaya, M.G.; Kasatkin, A.V.; Eremin, O.V. High-Temperature Crystal Chemistry of Meta-Autunite Group Minerals: Metatorbernite,  $\text{Cu}(\text{UO}_2)_2(\text{PO}_4)_2(\text{H}_2\text{O})_8$  and Metazeunerite,  $\text{Cu}(\text{UO}_2)_2(\text{AsO}_4)_2(\text{H}_2\text{O})_8$ . *Crystals* **2023**, *13*, 1688. <https://doi.org/10.3390/cryst13121688>

Academic Editor: Zhaohui Li

Received: 16 November 2023

Revised: 3 December 2023

Accepted: 13 December 2023

Published: 15 December 2023



**Copyright:** © 2023 by the authors. Licensee MDPI, Basel, Switzerland. This article is an open access article distributed under the terms and conditions of the Creative Commons Attribution (CC BY) license (<https://creativecommons.org/licenses/by/4.0/>).

**Keywords:** uranium minerals; metatorbernite group; metazeunerite; autunite-type layers; high-temperature crystal chemistry; thermal expansion

## 1. Introduction

Secondary uranium minerals of the meta-autunite group,  $M[(\text{UO}_2)_2(\text{TO}_4)_2] \cdot (8-12)\text{H}_2\text{O}$  ( $M = \text{K}, \text{Na}, \text{NH}_4, \text{H}_3\text{O}, \text{Ba}, \text{Ca}, \text{Co}, \text{Cu}, \text{Fe}^{2+}, \text{Mg}, \text{Mn}^{2+}, \text{Ni}, \text{Zn}$ ;  $T = \text{As}$  or  $\text{P}$ ) [1] are formed at various stages of oxidation of uranium deposit areas [2]. Some of them are of particular interest being present in amounts essential for industrial processing [3]. Due to the particularly low solubility in neutral solutions and omnipresence of phosphorus sources, uranyl phosphates are considered to play a very essential role in uranium migration both in geological media and in the environment of spent nuclear fuel (SNF) deposits [4]. For instance, in Finland and Sweden, SNF is packed into sealed copper vessels which slowly oxidize under ambient conditions; reaction with SNF leads to the formation, among others, of torbernite-like compounds [5,6].

By now, the meta-autunite group contains 21 mineral species whereof the most common are meta-autunite, metatorbernite, metazeunerite and their partially dehydrated derivatives [7]. These minerals generally form as well-faceted square platelets up to 1 mm in size. Unfortunately, these are generally not suitable for X-ray studies due to twinning and damage caused by metamict decay as well as by de- and rehydration processes. Structure investigation of meta-autunite group minerals was performed in four tetragonal, two monoclinic, and one triclinic space groups, most of which are subgroups of the  $P4/nmm$  which corresponds to the highest (archetypic) symmetry. All these structures belong to the same motif, wherein each uranium polyhedra (tetragonal bipyramid) shares equatorial vertices

with four  $TO_4$  ( $T = P, As$ ) polyhedra arranged in a checkerboard manner, thus forming autunite-like layers;  $H_2O$  molecules and cations are sandwiched in the interstices. The subtle structural differences, reflected in symmetry breaking from the archetypic  $P4/nmm$ , are due to variations in the arrangement and site occupancies of the interstitial species (metal cations and  $H_2O$  molecules), and rotations of U- and P- (or As-) centered polyhedra around the axes perpendicular to the autunite-type layers.

The “basic” structural models for the meta-autunite group minerals are those of autunite,  $Ca(UO_2)_2(PO_4)_2(H_2O)_{10-12}$  [8], and meta-autunite,  $Ca(UO_2)_2(PO_4)_2(H_2O)_6$  [9]. The structure of metatorbernite was initially solved in  $P4/nmm$  with the unit cell parameters of  $a = 6.95$ , and  $c = 17.26$  Å [9]; unfortunately, this model provided unrealistic anisotropic thermal parameters for oxygen atoms ( $R1 = 4.1\%$ ). Later, the space group and cell parameters were reconsidered several times. Ross et al. [10] and later Stergiou et al. [11] refined the structure in a similar unit cell ( $a = 6.969$ ,  $c = 17.306$  Å,  $R1 = 5.6\%$ ), but in another tetragonal  $P4/n$  space group. Based on IR spectroscopy data, Calos and Kennard [12] suggested a twice smaller unit cell ( $a = 6.950(1)$ ,  $c = 8.638(4)$  Å), and refined the structure in the  $P4/nmm$  space group to  $R1 = 9.2\%$ . In 2003, Locock and Burns [13] studied a synthetic analog of metatorbernite and demonstrated that the structure could be successfully refined both in  $P4/nmm$  and in  $P4/n$ , but finally chose in favor of the latter space group. Recent studies using synchrotron radiation indicated that this structure could be refined both in  $P4/n$  and in  $P4/ncc$  [14].

A similar diversity is observed for the structural model of metazeunerite. Its crystal structure was initially refined by Hanic [15] in the  $P4_2/nmc$  space group with  $R1 = 14.8\%$ . Hennig et al. [16] refined it in  $P4/ncc$ , ( $c = 17.420(1)$  Å) and  $P4/nmm$  ( $c = 8.710(1)$  Å). Locock and Burns [13] suggested  $P4/n$  with  $a = 7.1094(1)$  and  $c = 17.416(1)$  Å.

These controversies most likely occur from the fact that the hydration state of the mineral under study is variable and not always well known exactly for a given sample under conditions of current study; as previously noted, the variations in the arrangement of interlayer species, including  $H_2O$  molecules, subtle as they are, may affect the overall symmetry. For instance, torbernite,  $Cu(UO_2)_2(PO_4)_2(H_2O)_{12}$ , partially converts to metatorbernite,  $Cu(UO_2)_2(PO_4)_2(H_2O)_8$ , already at ambient conditions [17]. This fact is also confirmed by our studies, since most of the examined samples from the private and museum collections were actually dehydrated meta-forms regardless of what was indicated on the label. Thus, the water content is by no means constant and strongly depends on storage temperature, overall pressure, relative humidity, etc. [18]. The mineral may partially effloresce even upon mild heating by the incident X-ray beam [19]. Moreover, thermal analysis results are expected to differ for specimens taken from different deposits and localities, since metatorbernite samples from different sources could also exhibit different patterns of cation/ $H_2O$  distribution in the interlayer space [14]. This creates essential difficulties and uncertainties upon determination of not only the structural details, but also the thermal behavior and calculation of thermodynamic parameters for the minerals of the meta-autunite group. The latter data are essential for better understanding the genesis of some uranium deposits and prediction of uranium migration from natural and technogenic sources [4].

The differences in hydration states and overall interlayer arrangements are very well illustrated by the controversies in the published data on thermal behavior of various samples of the same minerals and their synthetic analogs. Upon thermal studies of metatorbernite, Frost et al. [20] observed four stages of mass loss at 295, 411, 428, and 564 K (the values are recalculated from °C given in the original paper) which they correlated to dehydration processes and stepwise release of 1.5, 4.5 and 2  $H_2O$  molecules per formula unit (*pfu*). Above 564 K, the named compound is anhydrous. According to the DTA studies by Pozas-Tormo et al. [21], metatorbernite dehydrates in four stages at 348, 383, 416, and 510 K, releasing 3  $H_2O$  molecule *pfu* between 298 and 353 K, five between 353 and 423 K, and two between 423 and 573 K. Studies by Ambartsumyan et al. [22] and Cejka et al. [23] revealed

endothermic events at nearly coinciding temperatures of 393, 423, and 528 K, and 406, 445, and 538 K, respectively.

Studies of synthetic metatorbernite crystals [24,25] revealed three steps of H<sub>2</sub>O loss: four molecule *pfu* below 393 K, two between 393 and 423 K, and another two between 423 and 723 K, corresponding to full dehydration. Further heating resulted in the formation of copper pyrophosphate and uranium oxide.

Similar contradictions also exist for metazeunerite. Frost et al. [17] recorded five dehydration stages at 321, 361, 398, 1155, and 1186 K. The first three correspond to the release of 2, 4, and 2 H<sub>2</sub>O molecule *pfu*, while the two latter stages may involve loss of arsenic and formation of anhydrous Cu[(UO<sub>2</sub>)(AsO<sub>4</sub>)<sub>2</sub>]<sub>2</sub>. Vochten et al. [25] conducted their TGA studies in air stream and reported four dehydration steps for a synthetic analog with formation of Cu(UO<sub>2</sub>)<sub>2</sub>(AsO<sub>4</sub>)<sub>2</sub>(H<sub>2</sub>O)<sub>7</sub> (at 381 K), Cu(UO<sub>2</sub>)<sub>2</sub>(AsO<sub>4</sub>)<sub>2</sub>(H<sub>2</sub>O)<sub>3</sub> (403 K), Cu(UO<sub>2</sub>)<sub>2</sub>(AsO<sub>4</sub>)<sub>2</sub>(H<sub>2</sub>O)<sub>2.5</sub> (458 K), and Cu(UO<sub>2</sub>)<sub>2</sub>(AsO<sub>4</sub>)<sub>2</sub> (503 K). Chernorukov et al. [26] noticed that between 323 and 473 K, metazeunerite releases H<sub>2</sub>O molecules in several steps at 333, 355, 381, 401, and 453 K.

Despite the detailed character of the aforementioned thermal studies of metatorbernite and metazeunerite, these data differ very essentially between each other; their thermal expansion was not addressed at all. Within the current study, we performed a combined single-crystal (SCXRD) and powder (PXRD) X-ray diffraction study to investigate the thermal expansion of these minerals, determine the components of the thermal expansion tensor, and to explain these observations based on atomic coordinates, bond distances, and angles. In a course of single-crystal studies, general attention was paid to the temperature intervals below the first dehydration stage where an H<sub>2</sub>O content of the samples under study is more or less constant. Above the first dehydration step, the crystals lost their integrity and the acquired data became uninterpretable. PXRD studies were conducted also at higher temperatures, in order to register the dehydration events.

## 2. Materials and Methods

### 2.1. Samples and Occurrence

The crystals of metatorbernite (**1**) were collected at the Old Gunnislake Mine, Clitters United Mines, Gunnislake, Calstock, Cornwall, England, UK. The crystals of metazeunerite (**2**) were collected at the Weißer Hirsch Mine, Neustädtel, Schneeberg, Erzgebirgskreis, Saxony, Germany (**2a**), and from Melekhinskaya Sopka, Sherlovaya Gora Deposit, Borzinsky District, Zabaykalsky Krai, Russian Federation [27] (**2b**). In the selected samples, metatorbernite associates mainly with meta-autunite, uraninite and cuprite. Metazeunerite in sample **2a** associates with trögerite, uranospinite and walpurgite, and sample **2b** is formed along cracks of quartz–topaz greisen with ferberite.

### 2.2. Chemical Composition

The semi-quantitative chemical analyses of **1** and **2** were carried out with a Hitachi FlexSEM 1000 scanning electron microscope (Tokyo, Japan) equipped with an EDS Xplore Contact 30 detector and Oxford AZtecLive STD system of analysis (Oxford, UK). Analytical conditions were as follows: accelerating voltage 20 kV and beam current 5 nA. The following standards and X-ray lines were used: Cu—Cu, K $\alpha$ ; Si—SiO<sub>2</sub>, K $\alpha$ ; P—NdP<sub>5</sub>O<sub>14</sub>, K $\alpha$ ; As—GaAs, L $\alpha$ ; U—UO<sub>2</sub>, M $\beta$ .

In sample **1**, only Cu, U and P were determined by EDS with a ratio 0.89:2.11:1.99; no admixture of As was found. In samples **2a** and **2b**, in turn, a small admixture of P was detected: the Cu, U, As, P ratios were 0.88:2.04:1.81:0.23 and 0.96:1.99:1.97:0.06, respectively.

### 2.3. Single-Crystal X-ray Diffraction Studies

Single-crystal X-ray diffraction (SCXRD) data of **1** and **2a** were collected using a Rigaku XtaLAB Synergy-S diffractometer (Tokyo, Japan) [28] equipped with a PhotonJet-S detector operating with MoK $\alpha$  radiation at 50 kV and 1 mA. A single crystal was chosen and more than a hemisphere of data collected with a frame width of 0.5° in  $\omega$ , and 3 s spent

counting for each frame. The data were integrated and corrected for absorption, applying a multi-scan-type model using the Rigaku Oxford Diffraction programs CrysAlisPro (Tokyo, Japan) [29].

The same crystals of **1** and **2a** were used in the temperature range of 100–300 K, using the Oxford Cryostream 800 system (Oxford, UK). The structures were successfully refined with the use of the SHELX software package [30]. Crystallographic data collected at 100 K are provided in Table 1. Supplementary crystallographic data were deposited in the Inorganic Crystal Structure Database (ICSD) and can be obtained by quoting CSD 2307946–2307947 via [www.ccdc.cam.ac.uk/structures](http://www.ccdc.cam.ac.uk/structures) (accessed on 1 October 2023).

**Table 1.** Crystallographic data and refinement parameters for **1** and **2a**.

	<b>1</b>	<b>2a</b>
Temperature (K)	100	
Radiation, $\lambda$ (Å)	MoK $\alpha$ , 0.71073	
Crystal system	tetragonal	
Space group	<i>P4/nmm</i>	
<i>a</i> (Å)	6.9589(2)	7.0896(2)
<i>c</i> (Å)	8.6170(4)	8.6802(5)
Volume (Å <sup>3</sup> )	417.29(3)	436.29(4)
Crystal size (mm <sup>3</sup> )	0.15 × 0.06 × 0.04	0.17 × 0.07 × 0.05
$\theta$ range (°)	3.76–27.50	3.71–28.39
<i>h, k, l</i> ranges	−8 → 7, −9 → 9, −8 → 11	−7 → 9, −8 → 9, −11 → 7
Total reflections collected	2058	1869
Unique reflections ( <i>R<sub>int</sub></i> )	0.038	0.045
<i>R</i> <sub>1</sub> [ <i>F</i> > 4 $\sigma$ <i>F</i> ], <i>wR</i> <sub>1</sub> [ <i>F</i> > 4 $\sigma$ <i>F</i> ]	0.021, 0.055	0.051, 0.13
<i>R</i> <sub>all</sub> , <i>wR</i> <sub>all</sub>	0.023, 0.056	0.058, 0.14
Highest difference peak	1.96	4.54
Deepest hole	−1.20	−2.46
Goodness-of-fit	1.089	1.118
ICSD	2307946	2307947

The effect of thermal motion on the bond length values from SCXRD experiments [31] was taken into account. Corrections for all bonds in the studied compounds were calculated by using a formula for the rigid-body motion:

$$L^2 = l_0^2 + \frac{3}{8} \pi^2 (B_{\text{eq}}(A_2) - B_{\text{eq}}(A_1))$$

where *L* and *l*<sub>0</sub> are corrected and observed *A*<sub>1</sub>–*A*<sub>2</sub> bond lengths, respectively; *B*<sub>eq</sub>(*A*<sub>1</sub>) and *B*<sub>eq</sub>(*A*<sub>2</sub>) are equivalent temperature factors of *A*<sub>1</sub> (cation, i.e., Cu or S) and *A*<sub>2</sub> (anion, i.e., O or Cl) atoms, respectively.

As noted above, two unit cell versions have been proposed for metatorbernite and metazeunerite with *c*~8.6 or 17 Å (double the first value), with the structures solved either in *P4/nmm* or in one of its subgroups. Structure solutions for synthetic analogs of metatorbernite and metazeunerite [13] were performed in *P4/n* using a [010/100/001] twin matrix. In fact, the structure of **1** can be considered as an alternation of autunite-like layers and layers formed by copper-centered polyhedra (vide infra). In the highest-symmetrical (*P4/nmm*) unit cell, two copper sublayers are repeated (Figure 1a); the unique copper site is

assumed to be half occupied. In the lower-symmetrical ( $P4/n$ ) structure, the copper cations and vacancies comprise two sites of twice lower occupancy (compared to the previous case) which are ordered (one fully occupied, one vacant) and shifted in the next layer in a staggered order to the former (Figure 1b). Therefore, the inter-autunite-layer contents in these structures exhibit different topologies. The projections of the U and T cations in the autunite-like layers onto representations of the  $P4/nmm$  and  $P4/n$  space groups are given in Figure 1c,d; the U and T cation positions are fixed irrespective of the space group choice. In the meantime, the positions of the copper and oxygen atoms are affected (Figure 1e,f). In the archetypic  $P4/nmm$  case, the copper atoms are located both at the planes and on the fourfold axes, while those of oxygen atoms are fixed at the symmetry planes. In the less symmetrical  $P4/n$ , the copper atoms reside only on the fourfold axes (the on-plane site is vacant). Overall, there exist two sites which could accommodate copper cations whereof only one is occupied in each of the two layers in  $P4/n$  solution.

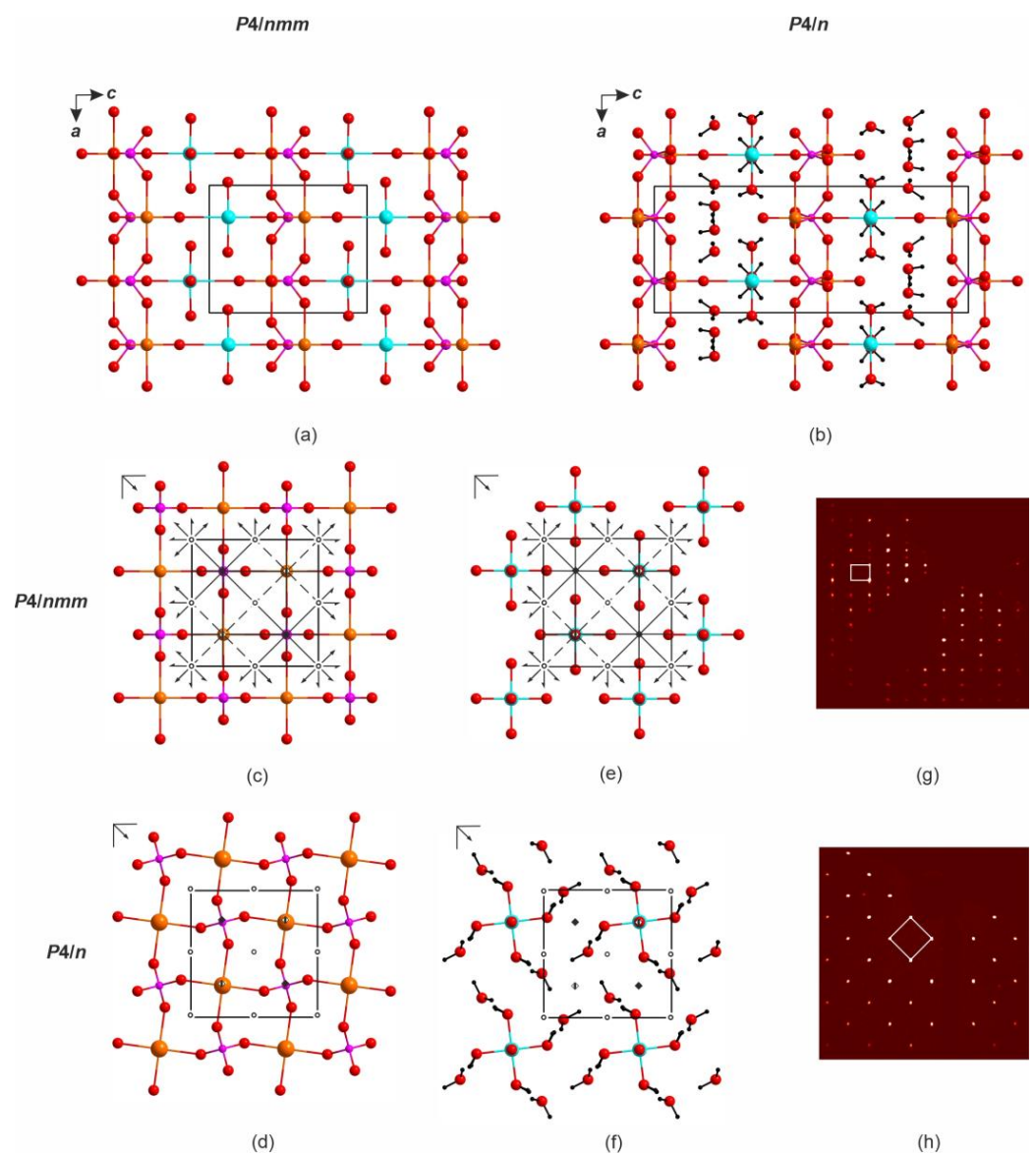


**Figure 1.** Projection of the structure of 1 in  $P4/nmm$  (a) and  $P4/n$  (b) along the [010] direction. Projection of the uranyl phosphate layers (c,d) and Cu-H<sub>2</sub>O (e,f) interstitial space in the structure of 1 in the  $P4/nmm$  and  $P4/n$  space groups, respectively. Unwrapped precession images of the reciprocal space along  $b^*$  (g) and  $c^*$  (h) of the structure of 1. Legend: U = brown; P = lilac; Cu = cyan; O = red; H = black.



Locock and Burns [13] pointed out that the introduction of twin matrices essentially affected the structure solution of synthetic analogs, permitted a double decrease in  $R1$  and resolved the problem of high residual electron density. We attempted to refine the structures of **1** and **2a** based on natural samples in all space groups hitherto reported for the meta-autunite group minerals; the best results were obtained for  $P4/nmm$  and  $P4/n$ . However, we were unable to attain  $R1$  values below 11% in  $P4/n$ , and the residual density peaks' values were too high ( $5.550/-4.720 \text{ e}/\text{\AA}^3$ ). Applying the twin matrix suggested by Locock and Burns [13] did not improve the solution. The solution in  $P4/n$  with a doubled cell parameter  $c$  ( $\sim 17 \text{ \AA}$ ) with the introduction of the  $[100/001/0-10]$  twin matrix resulted in the disappearance of residual density; yet, the search for higher symmetry using PLATON [32] indicated a likely space group,  $P4/ncc$ . Attempted refinement in the  $P4/ncc$  group resulted in non-realistic anisotropic thermal parameters of Cu and O (mostly non-positive definite). Therefore, we consider the solution in  $P4/nmm$  in the smaller unit cell, described above, as the most reliable. The reconstructed reciprocal space of **1** (Figure 1g,h) contains some additional reflections in  $(0kl)^*$  planes; these extra spots are either artifacts or consequences of the started dehydration processes.

#### 2.4. Powder X-ray Diffraction Studies at Non-Ambient Temperatures

Crystalline samples of **1**, **2a** and **2b** were ground in an agate mortar and prepared from heptane suspension on a Pt strip ( $20 \times 12 \times 2 \text{ mm}^3$ ) for the in situ examination using a Rigaku Ultima IV powder X-ray diffractometer (PXRD,  $\text{CuK}\alpha$  radiation; 40 kV/30 mA; Bragg-Brentano geometry; PSD D-Tex Ultra detector; Rigaku, Tokyo, Japan). A Rigaku R-300 chamber was used for data collection under vacuum within a range of 100–573 K with T steps of 10 K. A Rigaku SHT-1500 chamber (Rigaku, Tokyo, Japan) was used for data collection in air within a range of 293–673 K with T steps of 10 K. The heating rate was 2 K/min. The collection time at each temperature step was about 30 min. The zero-shift parameter was refined at every step, and it was usually increased by  $0.01\text{--}0.02^\circ 2\theta$  because of the sample holder expansion upon heating. Phases were identified using the ICDD PDF-2 Database (release 2019; Newtown Square, PA 19073, USA).

Several runs were performed to statistically confirm the obtained data. The unit cell parameters at different temperatures were calculated at every temperature step with the Rietveld method using the TOPAS program [33]. The ThetaToTensor program [34] was applied for the determination of the main coefficients of the thermal expansion tensor using a linear approximation of temperature dependences for the unit cell parameters, as well as for the determination of the principal axes of the thermal expansion tensor orientation.

#### 2.5. Thermodynamic Calculations

The equilibrium states of **1** and **2** under heating and atmospheric pressure were calculated in the Selector software package, based on minimizing the Gibbs energies of multicomponent multiphase systems [35]. Thermodynamic data for a variety of possible components are taken from reference books [36–38].

### 3. Results

#### 3.1. Crystal Structure Description

In the crystal structures of **1** and **2**, the single crystallographically non-equivalent U atom forms a typical uranyl cation ( $\langle \text{U-O}_{\text{Ur}} \rangle = 1.782$  and  $1.789 \text{ \AA}$ , respectively) which is coordinated, in the equatorial plane, via four O atoms ( $\langle \text{U-O}_{\text{eq}} \rangle = 2.273$  and  $2.260 \text{ \AA}$ ) (Figure 2a,b). One symmetrically independent T atom ( $T = \text{P, As}$ ) is tetrahedrally coordinated with  $\langle T-\text{O} \rangle = 1.509$  and  $1.631 \text{ \AA}$  for  $\text{PO}_4$  and  $\text{AsO}_4$ , respectively. The Cu atom is coordinated by six ligands, forming a distorted octahedron (4 + 2), due to the pronounced Jahn–Teller effect [39]. Each  $[\text{CuO}_2(\text{H}_2\text{O})_4]$  octahedron has two long ( $\langle \text{Cu-O} \rangle = 2.525$  and  $2.551 \text{ \AA}$ ) and four short ( $\langle \text{Cu-H}_2\text{O} \rangle = 1.911$  and  $1.950 \text{ \AA}$ ) bonds. In the structure of **2**, O sites in the equatorial plane of the  $\text{CuO}_6$  are split (Figure 2b). The bond valence sums, calculated using the parameters from [40], correlate well with the formal valences of the atoms.

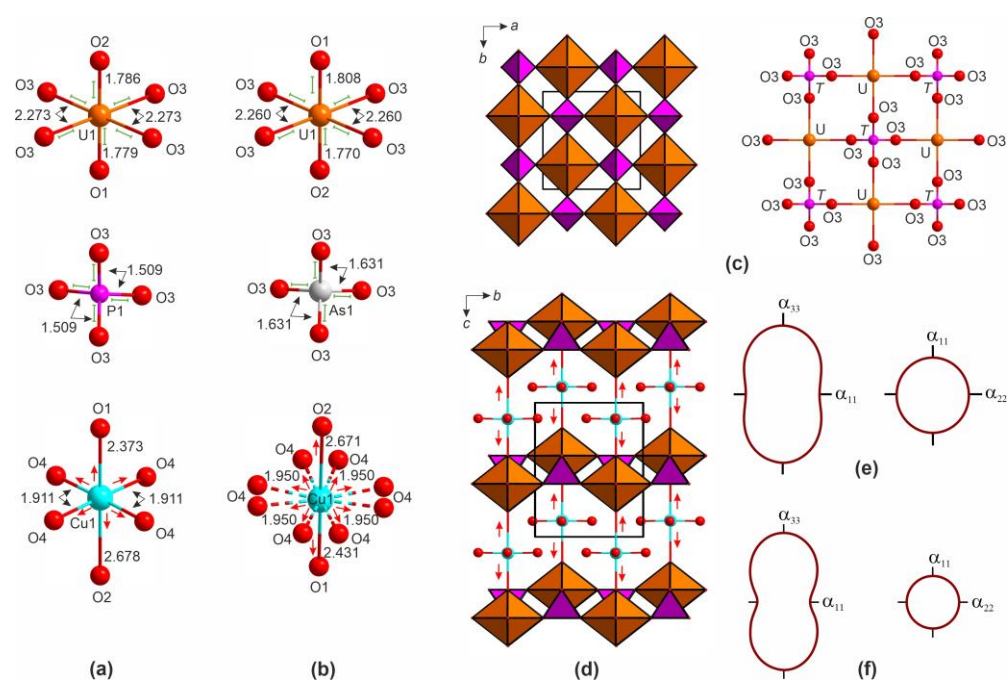


**Figure 2.** Thermal expansion of the crystal structures of **1** and **2**. Thermal behavior of U-, P-, As- and Cu-centered coordination polyhedra in the structures of **1** (a) and **2** (b); bond length values are given for the model at 100 K. Polyhedral and ball-and-stick representations of **1** and **2** along the [001] (c) and [100] (d) directions. The pole figures of thermal expansion coefficients of **1** (e) and **2** (f) in the temperature range of 100–300 K. Legend: see Figure 1; bonds that increases on heating are marked with red arrows, and those that do not change on heating are marked by green lines.

In the structures of **1** and **2** (Figure 2c), UO<sub>6</sub> polyhedra share vertices with the TO<sub>4</sub> (T = P, As) tetrahedra to form corrugated autunite-type [(UO<sub>2</sub>)<sub>2</sub>(TO<sub>4</sub>)<sub>2</sub>]<sup>2-</sup> layers originally described by Beintema [8]. The Cu sites are located in between the uranyl phosphate 2D complexes, so that [CuO<sub>2</sub>(H<sub>2</sub>O)<sub>4</sub>] polyhedra link the autunite-type layers into the framework structure (Figure 2d).

### 3.2. Thermal Behavior of Metatorbernite and Metazeunerite Crystal Structures

The structures of **1** and **2** expand along all directions upon heating from 100 to 300 K, but most strongly along *c* (Figure 3a,b). The thermal dependences of the unit cell parameters can be correctly approximated by the following linear fits (where *T* is temperature). For metatorbernite,  $a = 6.9506 + 0.57 \times 10^{-4} T$ ,  $c = 8.606 + 1.31 \times 10^{-4} T$ , and  $V = 415.77 + 132 \times 10^{-4} T$ . For metazeunerite,  $a = 7.0818 + 0.66 \times 10^{-4} T$ ,  $c = 8.6576 + 2.11 \times 10^{-4} T$ , and  $V = 434.19 + 188 \times 10^{-4} T$ . The thermal expansion of **1** and **2** is strongly anisotropic (Figure 2e,f), and the principal coefficients are  $\alpha_{11} = 8(2)$ ,  $\alpha_{33} = 15(6)$ ,  $\alpha_V = 32(8) \times 10^{-6} \text{ K}^{-1}$  for **1** and  $\alpha_{11} = 9(2)$ ,  $\alpha_{33} = 24(2)$ , and  $\alpha_V = 43(7) \times 10^{-6} \text{ K}^{-1}$  for **2**. The anisotropy of the overall thermal expansion is connected to the anisotropy in expansion of coordination polyhedra (Figure 3c,d). Upon heating from 100 to 300 K, U–O bonds elongate only slightly yet monotonously (by 0.004(8) in the uranyl cation and by 0.003(6) Å in the equatorial plane). The PO<sub>4</sub> tetrahedra are slightly more rigid compared to the AsO<sub>4</sub> (0.001(4) vs. 0.002(1) Å, respectively). The largest increments are observed for the copper polyhedra: the Cu–H<sub>2</sub>O bonds in **1** elongate by 0.007(8) Å, while in **2**, by 0.027(8) Å. The bonds with O<sub>Ur</sub> (Cu–O1 and Cu–O4) also elongate anisotropically (by 0.011(8) Å and 0.026(8) Å in **1**, and by 0.015(2) Å and 0.035(2) Å in **2**, respectively). Thus, the bond lengths in the UO<sub>6</sub> and TO<sub>4</sub> polyhedra remain constant within the precision limit while those in the [CuO<sub>2</sub>(H<sub>2</sub>O)<sub>4</sub>] octahedra expand noticeably, which causes expansion of the interlayer space until the first dehydration step.

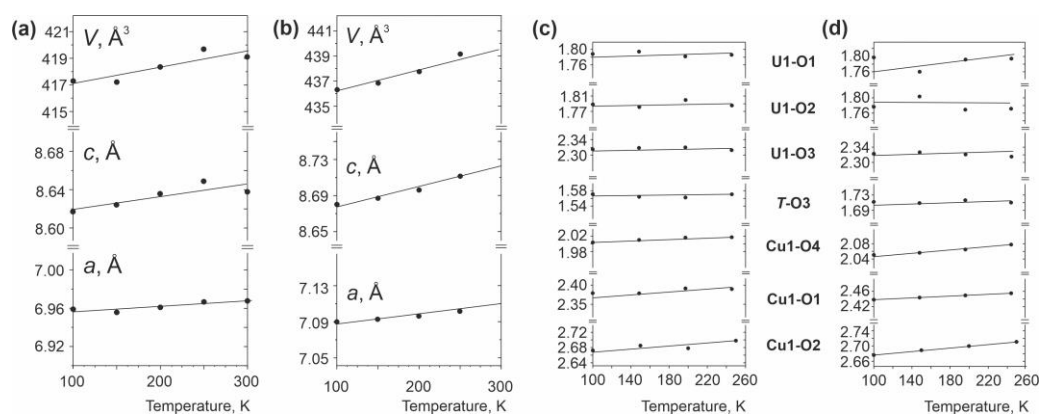


**Figure 3.** The unit cell parameters and selected bond lengths (Å) as a function of temperature (100–300 K) under heating for **1** (a,c) and **2** (b,d). ESDs of the unit cell and bond lengths parameters are within the limits of the symbols.

The evolution of PXRD patterns of **1** with a temperature increase in the range of 293–673 K is represented in Figure 4. Three dehydration stages (at 353, 373, and 483 K) are clearly visible in Figure 4a. Each step causes a shift in the diffraction maxima towards higher  $2\theta$  values, which is best illustrated by the (001) reflection. Stubbs et al. [41] calculated the interlayer distances from the positions of diffraction maxima and demonstrated that those expectedly decrease at each dehydration step. Due to high dehydration rates, the selection of monophasic products is a challenging task and many investigators have very likely dealt with mixtures of various hydrates. Heating such mixtures may result in two sets of reflections containing, e.g., initial **1** and its first dehydration product. Further heating of such mixtures leads to two transitions at 313 and 463 K. The temperatures of the first dehydration event, determined by the SCXRD and PXRD measurements, are in agreement.

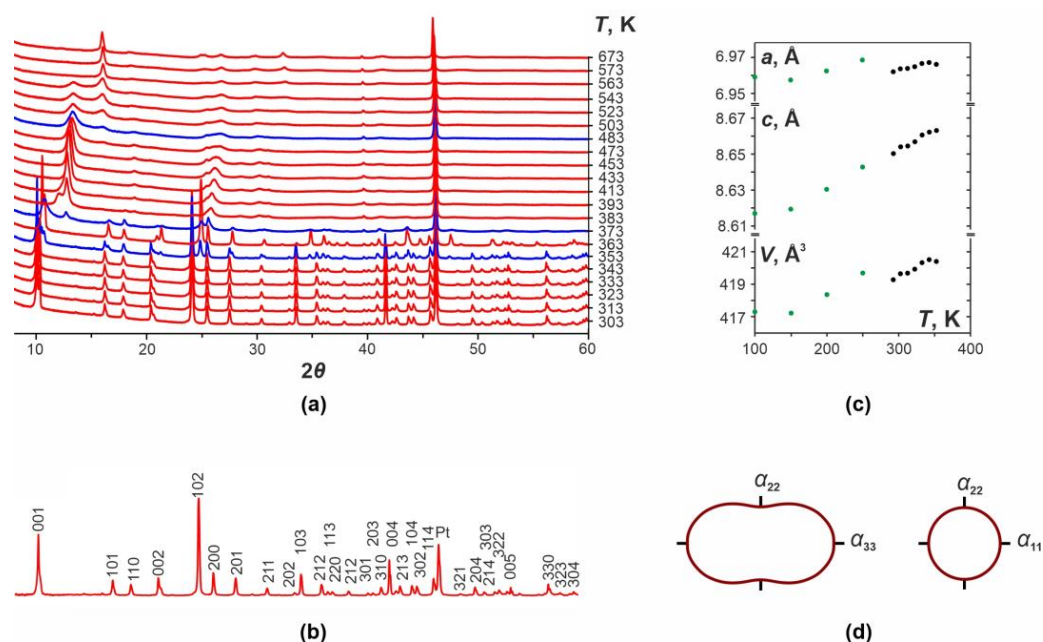


**Figure 4.** Powder X-ray diffraction patterns of **1** as a function of temperature (313–673 K) under heating in air (a). An experimental PXRD pattern for **1** collected at room temperature (b) with  $hkl$  indices marked. The unit cell parameters of metatorbernite as a function of temperature (c). PXRD experimental points are highlighted in black; SCXRD points are highlighted in green. The pole figures of thermal expansion coefficients of metatorbernite (d) in the temperature range of 313–353 K. The temperatures corresponding to the stages of dehydration are indicated in blue.



It can be seen from Figure 4a that the diffraction maxima of **1** mostly disappear at  $\sim 373$  K; the decomposition starts at  $\sim 353$  K. An experimental PXRD pattern for **1** at room temperature is shown in Figure 4b.

Equations describing the temperature dependence of the unit cell parameters of metatorbernite can be described by the following linear functions (where  $T$  is a temperature):  $a = 6.96 + 0.8 \times 10^{-4} T$ ;  $c = 8.65 + 2.17 \times 10^{-4} T$ ;  $V = 418.94 + 201.96 \times 10^{-4} T$ . Upon heating, the unit cell of **1** is expanding along all crystallographic axes (Figure 4c). PXRD experimental points are highlighted in black, SCXRD points are highlighted in green. The calculated values of the main components of the TE tensor ( $\alpha_{11} = 12(2)$ ,  $\alpha_{33} = 25(2)$ ,  $\alpha_V = 48(6) \times 10^{-6} \text{ K}^{-1}$ ) illustrate its strongly anisotropic character ( $\alpha_{\max}/\alpha_{\min} = 2.1$ ). The maximal thermal expansion is observed in the direction normal to the autunite-like layers (Figure 4d), which is in agreement with the SCXRD data.

The thermal behavior of **2** was studied in the range of 93–573 K (Figure 5a); the experimental PXRD pattern collected at 93 K is shown on Figure 5b. Between 93 and 283 K, the diffraction maxima shift only slightly due to the thermal expansion. The first event is observed at 283 K, while the second at 543 K. Another independent experiment between 100 and 333 K gives the same result. At c.a. 333 K, the diffraction pattern corresponds to a partially dehydrated phase which is stable until the end of experiment.

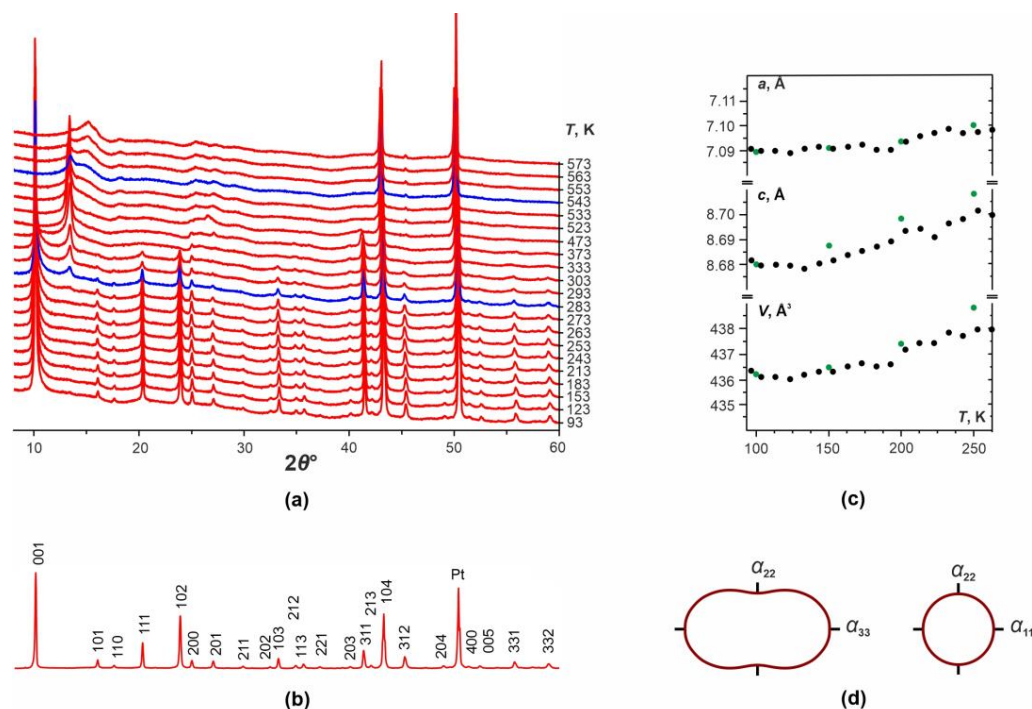


**Figure 5.** Powder X-ray diffraction patterns of **2** as a function of temperature (93–573 K) under heating in a vacuum (a). An experimental PXRD pattern for **2** collected at 93 K (b) with  $hkl$  indices marked. The unit cell parameters of metatorbernite as a function of temperature (c). PXRD experimental points are highlighted in black, SCXRD points are highlighted in green. The pole figures of thermal expansion coefficients of metatorbernite (d) in the temperature range of 100–263 K.

Equations describing the temperature dependence of the unit cell parameters of metazeunerite within the range of 100 to 263 K (Figure 5c) are  $a = 7.09 + 0.6 \times 10^{-4} T$ ,  $c = 8.7 + 1.52 \times 10^{-4} T$ , and  $V = 438.55 + 154 \times 10^{-4} T$ . The thermal expansion of **2** is strongly anisotropic ( $\alpha_{11} = 8(1)$ ,  $\alpha_{33} = 18(1)$ , and  $\alpha_V = 35(3) \times 10^{-6} \text{ K}^{-1}$ ). The maximal expansion is observed along the normal to the uranyl arsenate layers (Figure 5d), as it was observed for **1**.

Two independent methods (SCXRD and PXRD) were used to study the thermal expansion of metatorbernite and metazeunerite. The data obtained for each mineral (Figures 4c and 5c) were combined and utilized to calculate the average values of the

thermal expansion coefficients. ( $\alpha_{11} = 5(1)$ ,  $\alpha_{33} = 23(1)$ , and  $\alpha_V = 32(3)$ ; and  $\alpha_{11} = 9(1)$ ,  $\alpha_{33} = 17(1)$ ,  $\alpha_V = 34(3) \times 10^{-6} \text{ K}^{-1}$  for **1** and **2**, respectively). Yet, the caveat is that the two parts of this graph contain data obtained using different techniques, including calculation methods, and therefore different levels of precision.

### 3.3. Changes in the Standard Gibbs Energies of Formation Calculations

Expansions of the  $\Delta_f G^\circ$  values into oxide components are obtained [42,43] for the experimentally determined standard Gibbs energies of formations ( $\Delta_f G^\circ$ ) of synthetic metatorbernite [44] and metazeunerite [45] as follows according to Table 2:

$$\Delta_f G^\circ(\mathbf{1}) = g(\text{CuO}) + 8g(\text{H}_2\text{O}) + 2g(\text{UO}_3) + g(\text{P}_2\text{O}_5) = -6132.0 \text{ (kJ/mol)}, \quad (1)$$

$$\Delta_f G^\circ(\mathbf{2}) = g(\text{CuO}) + 8g(\text{H}_2\text{O}) + 2g(\text{UO}_3) + g(\text{As}_2\text{O}_5) = -5356.0 \text{ (kJ/mol)}, \quad (2)$$

**Table 2.** Additive oxide contributions of the  $\Delta_f G^\circ$  values of metatorbernite (**1**) and metazeunerite (**2**).

Compound	$g(\text{CuO})$ , kJ/mol	$g(\text{H}_2\text{O})$ , kJ/mol	$g(\text{UO}_3)$ , kJ/mol	$g(\text{T}_2\text{O}_5)$ , $T = \text{P, As}$ , kJ/mol
<b>1</b>	−238.573	−239.035	−1240.771	−1499.603
<b>2</b>	−178.408	−259.211	−1142.566	−818.766

The contributions of the oxides  $g(\text{P}_2\text{O}_5)$  and  $g(\text{As}_2\text{O}_5)$  to the  $\Delta_f G^\circ$  values differ significantly (Table 2), since they represent properties for different chemical elements. Taking into account the identical stoichiometry of metatorbernite and metazeunerite, one can compare the values of  $g(\text{CuO}) + 8g(\text{H}_2\text{O}) + 2g(\text{UO}_3)$  for decompositions (**1**) and (**2**). They are −4632.395 and −4537.228 kJ/mol, respectively, which shows a greater energetic affinity for the complexation of uranium oxides, copper and water with phosphate than with arsenate. According to the polythermic studies, reported both in previous and our studies, thermal dehydration results in the formation of anhydrous copper uranyl phosphate and arsenate, respectively, which are in turn stable to relatively high temperatures. Unfortunately, no thermodynamic data are known for these complex compounds. Therefore, only qualitative trends can be compared when considering the stability of hydrated species against simple constituting oxides.

## 4. Discussion

Despite the essential spread of temperature ranges for the dehydration steps of metatorbernite, most investigators point to three intervals of 373–393, 393–423, and 503–523 K. Our data on the first step agree well with the values reported by Pozas-Tormo (383 K) [21], Ambartsumyan (383 K) [22], and Vochten (393 K) [24], which are 10–30 K below those reported by Frost (411 K) [20] and Stubbs (402 K) [43]. According to the TGA data, metatorbernite releases from 1.5 [20] to 4 [24]  $\text{H}_2\text{O}$  molecule *pfu*. In experiments performed on pure metatorbernite (without dehydrated phases), no effects are registered at other temperatures, in contrast to those at 423–453 K reported by Vochten et al. [24]. In addition, we did not observe any effects at 295 upon heating pure metatorbernite. In the meantime, experiments performed on mixtures of pristine and partially dehydrated metatorbernite two effects at 303 and 473 K were registered. These “extra” events may occur either due to the earlier overcoming of kinetic barriers or the formation of intermediate hydrates via “seeded” dehydration.

The study of **2** by variable-temperature PXRD reveals two dehydration steps at 283 and 543 K. Close values to the first were reported by Frost (321 K) and Chernorukov (333 K), and to the second by Vochten (503 K). The changes in diffraction pattern are smooth, and some maxima disappear between 283 and 373 K.

We note that the registered temperatures of the first dehydration effect in our single-crystal and powder diffraction experiments nearly coincide (300–363 and 250–303 K for

**1** and **2**, respectively). However, the thermal behavior of both isostructural minerals is different. The reasons likely stem from the structural details: the autunite-like layers in their structures are comprised of vertex-sharing  $\text{UO}_6$  octahedra and  $\text{TO}_4$  tetrahedra, via the  $\text{U-O3-T}$  bridges (Figure 2c). The  $\text{U-O3}$  distance increases by 0.003(6) Å for **1** and by 0.006(2) Å in **2** with an average length of 2.320 Å with increasing temperature. The  $\text{P-O3}$  and  $\text{As-O3}$  increase by 0.001(4) and 0.002(1) Å with the average lengths of 1.567 and 1.710 Å in **1** and **2**, respectively. Hence, the longer  $\text{As-O3}$  exhibits a slightly larger thermal expansion as compared to the shorter  $\text{P-O3}$ . This is reflected in the small but statistically discernable differences of thermal expansion coefficients in the plane of the layer ( $\alpha_{11} = 8(2)$  and  $9(2) \times 10^{-6} \text{ K}^{-1}$  for **1** and **2**, respectively). The expansion in the normal direction is of the same order ( $\alpha_{33} = 15(6)$  and  $24(2) \times 10^{-6} \text{ K}^{-1}$ , respectively); it is mostly determined by the expansion of  $\text{CuO}_6$  polyhedra. The latter are linked to the autunite layers via  $\text{O1-Cu1-O2}$  bridges (Figure 2c). In the equatorial plane, each Cu cation forms four  $\text{Cu-O4}$  bonds. The  $\text{Cu1-O1}$  distances increase by 0.010(8) and 0.015(2) Å upon heating, while  $\text{Cu1-O2}$  by 0.025(8) and 0.035(2) Å for **1** and **2**, respectively. The equatorial  $\text{Cu-O4}$  bonds elongate by 0.014(8) and 0.027(2) Å. Therefore, an expansion of interstitial structure, which includes  $\text{CuO}_6$  octahedra, is nearly two orders larger compared to those in the autunite-like layers; the equatorial  $\text{Cu-O4}$  bonds expand twice more rapidly in **2** compared to **1**, which explains the differences in the  $\alpha_{33}$  values.

## 5. Conclusions

In this paper, we reported on the thermal behavior studies of the crystal structures of two related uranyl minerals, metatorbernite and metazeunerite, by the means of single-crystal and powder X-ray diffraction methods for the first time.

In terms of thermal behavior, the structure of metatorbernite can be considered as a system of one rigid and other “inflatable” layers (comprised of  $\text{UO}_6$ - $\text{PO}_4$  and  $\text{CuO}_6$  polyhedra) wherein heating leads to increasing interlayer distance which enhances the stepwise release of water. The structure of metazeunerite is more flexible due to the larger expansion of the  $\text{AsO}_4$  tetrahedra; this may possibly account for the partial retention of  $\text{H}_2\text{O}$  molecules between 283 and 543 K.

An important point when studying minerals of this group is the choice of the unit cell and the space symmetry group. A “direct”, “intuitive”, or “by-analogy-to” attribution of a mineral to a particular space group in this family is apparently incorrect. Various settings should be considered as “polytype” modifications [46], for which the maximal symmetry will correspond to a small tetragonal unit cell with  $c \sim 8.6$  Å and the archetypic  $P4/nmm$  space group. The symmetry lowering can be caused by various factors, such as isomorphism in tetrahedral positions, different compositions of the interstitial complex, changes in the hydration degree during crystal growth, etc. Also note the possibility of subtle temperature- or composition-driven second-order phase transitions which are particularly challenging to detect. Yet, it should be noted that slight differences in chemical composition of **2a** and **2b** samples had no effect on the symmetry. The comparison of our results to those of the previous works indicates that the symmetry is mostly determined by the arrangement of Cu atoms. One is tempted therefore to assume that in synthetic crystals, these actually occupy only one of several potential sites [13], possibly due to some kinetic preferences, as the synthesis time is relatively short. For the natural samples, much longer formation times are sufficient for various re-distributions, including those leading to a higher overall symmetry and a smaller unit cell. On the other hand, there are many more parameters quite different for the natural and synthetic conditions, including different precursors, their chemical composition, impurity effects, etc. To elucidate their role and to determine which of these play the major role(s) in the resulting structural architecture of meta-autunite group minerals, further precise investigation of mineral species and synthetic phases is required.

**Author Contributions:** Conceptualization, E.V.N., V.V.G. and A.V.K.; Methodology, E.V.N. and V.V.G.; Software, E.V.N., Y.G.T., O.V.E. and M.G.K.; Validation, E.V.N.; Formal analysis, E.V.N., Y.G.T., A.V.K. and O.V.E.; Investigation, E.V.N., V.V.G., Y.G.T., D.O.C., M.G.K. and O.V.E.; Resources, A.V.K.; Data curation, Y.G.T. and A.V.K.; Writing—original draft, E.V.N., V.V.G. and D.O.C.; Writing—review and editing, E.V.N., V.V.G. and D.O.C.; Visualization, Y.G.T., E.V.N. and M.G.K.; Supervision, E.V.N. and V.V.G. All authors have read and agreed to the published version of the manuscript.

**Funding:** This research was funded by the Russian Science Foundation, grant number 23-17-00080.

**Data Availability Statement:** The data presented in this study are available in the article.

**Acknowledgments:** We are grateful to the reviewers for their valuable comments and personally to Borisov A.S. for his contribution to the experimental part of this work. Technical support by the X-ray Diffraction Resource Centers of Saint-Petersburg State University is gratefully acknowledged.

**Conflicts of Interest:** The authors declare no conflict of interest.

## References

1. Krivovichev, S.V.; Plášil, J. Mineralogy and Crystallography of Uranium. In *Uranium: From Cradle to Grave*; MAC Short Courses; Burns, P.C., Sigmon, G.E., Eds.; Midlands Arts Centre: Birmingham, UK, 2013; Volume 43, pp. 15–119.
2. Lussier, A.J.; Lopez, R.A.K.; Burns, P.C. A revised and expanded structure hierarchy of natural and synthetic hexavalent uranium compounds. *Can. Mineral.* **2016**, *54*, 177–283. [[CrossRef](#)]
3. Cuney, M.; Kyser, K. *Recent and Not-So-Recent Developments in Uranium Deposits and Implications for Exploration*; Mineralogical Association of Canada: Quebec City, QC, Canada, 2008.
4. Cretaz, F.; Szenknect, S.; Clavier, N.; Vitorge, P.; Mesbah, A.; Descostes, M.; Poinssot, C.; Dacheux, N. Solubility properties of synthetic and natural meta-torbernite. *J. Nucl. Mater.* **2013**, *442*, 195–207. [[CrossRef](#)]
5. Hedman, T.; Nystrom, A.; Thegerstrom, C. Swedish containers for disposal of spent nuclear fuel and radioactive waste. *Comptes Rendus Phys.* **2002**, *3*, 903–913. [[CrossRef](#)]
6. Rosborg, R.; Werme, L. The Swedish nuclear waste program and the long-term corrosion behaviour of copper. *J. Nucl. Mater.* **2008**, *379*, 142–153. [[CrossRef](#)]
7. Finch, R.; Murakami, T. Systematics and paragenesis of uranium minerals. In *Uranium: Mineralogy, Geology and the Environment*; Burns, P.C., Finch, R., Eds.; Mineralogical Society of America: Washington, DC, USA, 1999; pp. 91–179.
8. Beintema, J. On the composition and crystallography of autunite and the meta-autunites. *Recl. Trav. Chim. Pays Bas.* **1938**, *57*, 155–175. [[CrossRef](#)]
9. Makarov, E.S.; Tobelko, K.I. Crystal structure of metatorbernite. *Dokl. Akad. Nauk SSSR* **1960**, *131*, 87–89.
10. Ross, M.; Evans, H.T.; Appleman, D.E. Studies of the torbernite minerals. II. The crystal structure of meta-torbernite. *Am. Mineral.* **1964**, *49*, 1603–1621.
11. Stergiou, A.C.; Rentzeperis, P.J.; Sklavounos, S. Refinement of the crystal structure of metatorbernite. *Z. Kristallogr.* **1993**, *205*, 1–7. [[CrossRef](#)]
12. Calos, N.J.; Kennard, C.H.L. Crystal structure of copper bis(uranyl phosphate) octahydrate (metatorbernite),  $\text{Cu}(\text{UO}_2\text{PO}_4)_2 \times 8(\text{H}_2\text{O})$ . *Z. Kristallogr.* **1996**, *211*, 701–702. [[CrossRef](#)]
13. Locock, A.J.; Burns, P.C. Crystal structures and synthesis of the copper-dominant members of the autunite and meta-autunite groups: Torbernite, zeunerite, metatorbernite and metazeunerite. *Can. Miner.* **2003**, *41*, 489–502. [[CrossRef](#)]
14. Kulaszewska, J.; Dann, S.; Warwick, P.; Kirk, C. Solid solution formation in the metatorbernite–metazeunerite system  $(\text{Cu}(\text{UO}_2)_2(\text{PO}_4)_2 - x(\text{AsO}_4)_x \cdot n\text{H}_2\text{O})$  and their stability under conditions of variable temperature. *Phil. Trans. R. Soc.* **2018**, *377*, 20180242. [[CrossRef](#)] [[PubMed](#)]
15. Hanic, F. The crystal structure of meta-zeunerite  $\text{Cu}(\text{UO}_2)_2(\text{AsO}_4)_2 \times 8(\text{H}_2\text{O})$ . *Czech. J. Phys.* **1960**, *B10*, 169–181. [[CrossRef](#)]
16. Hennig, C.; Reck, G.; Reich, T.; Rossberg, A.; Kraus, W.; Sieler, J. EXAFS and XRD investigations of zeunerite and meta-zeunerite. *Z. Kristallogr.* **2003**, *218*, 37–45. [[CrossRef](#)]
17. Frost, R.L.; Weier, M.L.; Adebajo, M.O. Thermal decomposition of metazeunerite—A high-resolution thermogravimetric and hot-stage Raman spectroscopic study. *Thermochim. Acta* **2004**, *419*, 119–129. [[CrossRef](#)]
18. Suzuki, Y.; Sato, T.; Isobe, H.; Kogure, T.; Murakami, T. Dehydration processes in the meta-autunite group minerals meta-autunite, metasaléite, and metatorbernite. *Amer. Mineral.* **2005**, *90*, 1308–1314. [[CrossRef](#)]
19. Locock, A.J. Crystal chemistry of actinide phosphates and arsenates. In *Structural Chemistry of Inorganic Actinide Compounds*; Krivovichev, S.V., Burns, P.C., Tananaev, I.G., Eds.; Elsevier: Amsterdam, The Netherlands, 2007; pp. 217–278.
20. Frost, R.L.; Kristóf, J.; Weier, M.L.; Martens, W.N.; Horváth, E. Thermal decomposition of metatorbernite—A controlled rate thermal analysis study. *J. Therm. Anal. Calorim.* **2005**, *79*, 721–725. [[CrossRef](#)]
21. Pozas-Tormo, R.; Moreno-Real, L.; Martínez-Lara, M.; Bruque-Gamez, S. Layered metal uranyl phosphates. Retention of divalent ions by amine intercalates of uranyl phosphates. *Can. J. Chem.* **1986**, *64*, 30. [[CrossRef](#)]
22. Ambartsumyan, T.L.; Basalova, G.I.; Gorzhevskaya, S.A. *Thermal Investigations of Uranium and Uranium-Bearing Minerals*; Gosatomizdat: Moscow, Russia, 1961; 148p. (In Russian)



23. Cejka, J.; Muck, A. Thermal analysis and infrared spectra of some natural and synthetic uranium micas. *Thermochim. Acta* **1985**, *86*, 387. [[CrossRef](#)]
24. Vochten, R.; Huybrechts, W.; Remaut, G.; Deliens, M. Formation of meta-torbernite starting from curite: Crystallographic data and electrokinetic properties. *Phys. Chem. Miner.* **1979**, *4*, 281–290. [[CrossRef](#)]
25. Vochten, R.; Piret, P.; Goeminne, A. Synthesis, crystallographic data, solubility and electrokinetic properties of copper-, nickel- and cobalt-uranlyphosphate. *Bull. Minéral.* **1981**, *104*, 457–467. [[CrossRef](#)]
26. Chernorukov, N.G.; Nipruk, O.V.; Knyazev, A.V.; Pykhova, Y.P. Synthesis and study of uranyl arsenate  $(\text{UO}_2)_3(\text{AsO}_4)_2 \times 12\text{H}_2\text{O}$ . *Z. Neorg. Khim.* **2011**, *56*, 199–203. [[CrossRef](#)]
27. Filenko, R.A.; Yurgenson, G.A.; Smirnova, O.K. New data on mineralogy of the oxidation zone of the Sherlovogorsky ore area (Eastern Transbaikalia). *Geosph. Res.* **2018**, *4*, 44–55. [[CrossRef](#)]
28. Fraser, W. Diffractometers for modern X-ray crystallography: The XtaLAB Synergy X-ray diffractometer platform. *Rigaku J.* **2020**, *36*, 37–47.
29. *CrysAlisPro Software System*, version 1.171.41.94a; Rigaku Oxford Diffraction: Oxford, UK, 2021.
30. Sheldrick, G.M. Crystal structure refinement with SHELXL. *Acta Crystallogr.* **2015**, *C71*, 3–8.
31. Downs, R.T. Analysis of harmonic displacement factors. *Rev. Mineral. Geochem.* **2000**, *41*, 61–87.
32. Spek, A.L. An overview of PLATON/PLUTON crystal structure validation. *Acta Cryst.* **2020**, *E76*, 1–11. [[CrossRef](#)]
33. *Bruker TOPAS*, version 5.0; Bruker AXS Inc.: Madison, WI, USA, 2014.
34. Bubnova, R.S.; Firsova, V.A.; Filatov, S.K. Software for determining the thermal expansion tensor and the graphic representation of its characteristic surface (theta to tensor-TTT). *Glass Phys. Chem.* **2013**, *39*, 347–350. [[CrossRef](#)]
35. Chudnenko, K.V. *Thermodynamic Modeling in Geochemistry: Theory, Algorithms, Software, Applications*; Academic Publishing House Geo: Novosibirsk, Russia, 2010; 287p. (In Russian)
36. Grenthe, I.; Gaona, X.; Plyasunov, A.V.; Rao, L.; Runde, W.H.; Grambow, B.; Konings, R.J.M.; Smith, A.L.; Moore, E.E. *Second Update on the Chemical Thermodynamics of Uranium, Neptunium, Plutonium, Americium and Technetium, Chemical Thermodynamics*; Nuclear Energy Agency, OECD: Paris, France, 2021; Volume 14.
37. Yokokawa, H. Tables of thermodynamic properties of inorganic compounds. *J. Nation. Chem. Lab. Ind.* **1988**, *83*, 27–118.
38. Reid, R.; Prausnitz, J.; Sherwood, T. *The Properties of Gases and Liquids*, 3rd ed.; McGrawHill Book Company: New York, NY, USA, 1977; 592p.
39. Burns, P.C.; Hawthorne, F.C. Coordination-geometry structural pathways in  $\text{Cu}^{2+}$  oxysalt minerals. *Can. Mineral.* **1995**, *33*, 889–905.
40. Gagne, O.C.; Hawthorne, F.C. Bond-length distributions for ions bonded to oxygen: Alkali and alkaline-earth metals. *Acta Crystallogr. Sect. B Struct. Sci.* **2016**, *72*, 602–625. [[CrossRef](#)]
41. Stubbs, J.E.; Post, J.E.; Elbert, D.C.; Heaney, P.J.; Veblen, D.R. Uranyl phosphate sheet reconstruction during dehydration of metatorbernite  $[\text{Cu}(\text{UO}_2)_2(\text{PO}_4)_2 \cdot 8\text{H}_2\text{O}]$ . *Amer. Mineral.* **2010**, *95*, 1132–1140. [[CrossRef](#)]
42. Eremin, O.V. Method for calculating changes in the standard Gibbs energies of formation of minerals that belong to the class of uranophosphates. *Radiochemistry* **2020**, *62*, 480–491. [[CrossRef](#)]
43. Eremin, O.V.; Rusal', O.S.; Solodukhina, M.A.; Epova, E.S. Procedure for calculating the standard Gibbs potentials of minerals of the class of uranoarsenates. *Russ. J. Phys. Chem. A* **2020**, *94*, 678–686. [[CrossRef](#)]
44. Nipruk, O.V.; Chernorukov, N.G.; Godovanova, N.S.; Arova, M.I. State of uranophosphates  $\text{M}^{\text{II}}(\text{PUO}_6)_2 \cdot n\text{H}_2\text{O}$  ( $\text{M}^{\text{II}} = \text{Mn}^{2+}, \text{Co}^{2+}, \text{Ni}^{2+}, \text{Cu}^{2+}, \text{Zn}^{2+}, \text{Cd}^{2+}, \text{Pb}^{2+}$ ) in aqueous solutions. *Radiochemistry* **2012**, *54*, 528–536. [[CrossRef](#)]
45. Chernorukov, N.G.; Nipruk, O.V.; Pykhova, Y.P.; Godovanova, N.S. Study of the state of uranoarsenates  $\text{M}^{\text{II}}(\text{PUO}_6)_2 \cdot n\text{H}_2\text{O}$  ( $\text{M}^{\text{II}} = \text{Mn}^{2+}, \text{Co}^{2+}, \text{Ni}^{2+}, \text{Cu}^{2+}, \text{Zn}^{2+}, \text{Cd}^{2+}, \text{Pb}^{2+}$ ) in aqueous solutions. *Russ. J. Gen. Chem.* **2012**, *82*, 1348–1356. [[CrossRef](#)]
46. Moroz, I.K.; Valueva, A.A.; Sidorenko, G.A.; Zhil'tsova, I.G.; Karpova, L.N. The crystal chemistry of uranium micas. *Geokhimiya* **1973**, *18*, 210–223. (In Russian)

**Disclaimer/Publisher's Note:** The statements, opinions and data contained in all publications are solely those of the individual author(s) and contributor(s) and not of MDPI and/or the editor(s). MDPI and/or the editor(s) disclaim responsibility for any injury to people or property resulting from any ideas, methods, instructions or products referred to in the content.